Gapless Dirac surface states in the antiferromagnetic topological insulator MnBi_{2}Te_{4}

Przemyslaw Swatek, Yun Wu, Lin-Lin Wang, Kyungchan Lee, Benjamin Schrunk, Jiaqiang Yan, and Adam Kaminski

Phys. Rev. B **101**, 161109 — Published 16 April 2020

DOI: 10.1103/PhysRevB.101.161109

Gapless Dirac surface states in the antiferromagnetic topological insulator $MnBi_2Te_4$

Przemyslaw Swatek,[1,2] Yun Wu,[1,2] Lin-Lin Wang,[1] Kyungchan Lee,[1,2]
Benjamin Schrunk,[1,2] Jiaqiang Yan,[3,4,*] and Adam Kaminski[1,2,†]

[1] *Division of Materials Science and Engineering, Ames Laboratory, Ames, Iowa 50011, USA*
[2] *Department of Physics and Astronomy, Iowa State University, Ames, Iowa 50011, USA*
[3] *Materials Science and Technology Division, Oak Ridge National Laboratory, Oak Ridge, Tennessee 37831, USA*
[4] *Department of Materials Science and Engineering, University of Tennessee, Knoxville, Tennessee 37996, USA*

We used angle-resolved photoemission spectroscopy (ARPES) and density functional theory (DFT) calculations to study the electronic properties of $MnBi_2Te_4$, a material that was predicted to be an intrinsic antiferromagnetic (AFM) topological insulator. In striking contrast to the earlier literatures showing a full gap opening between two surface band manifolds on the (0001) surface, we observed a gapless Dirac surface state with a Dirac point sitting at E_B = -280 meV. Furthermore, our ARPES data revealed the existence of a second Dirac cone sitting closer to the Fermi level. Surprisingly, these surface states remain intact across the AFM transition. Presence of gapless Dirac states in this material may be caused by different ordering at the surface from the bulk or weaker magnetic coupling between bulk and surface. Whereas the surface Dirac cones seem to be remarkably insensitive to the AFM ordering most likely due to weak coupling to magnetism, we did observe a splitting of the bulk band accompanying the AFM transition. With a moderately high ordering temperature and interesting gapless Dirac surface states, $MnBi_2Te_4$ provides a unique platform for studying the interplay between magnetic ordering and topology.

The discovery of topological states such as Dirac/Weyl/Majorana fermion states in semimetals has ignited intensive studies [1–7]. Besides their unprecedented importance for understanding fundamental relativistic physics, they also offer intriguing possibilities for device applications revolutionizing computational as well as laser technologies [8]. Among them, magnetic topological semimetals and insulators are promising materials for spintronics, especially in the context of the new generation of logic or memory devices [9–12].

Antiferromagnetic topological insulators (AFM-TI) constitute a unique subclass of topological quantum materials with additional magnetic degrees of freedom [13, 14]. Instead of being protected by time-reversal symmetry (TRS) alone like in conventional TIs [1], surface states in AFM-TI can be protected by non-unitary $S = \Theta T_{1/2}$ symmetry, a combination of TRS Θ and nonsymmorphic translational $T_{1/2}$. The preservation of S symmetry provides surface states a protection from backscattering by a non-trivial Z_2 topology even if the material is in the magnetic states (i.e. TRS is broken). On the other hand, breaking the $T_{1/2}$ symmetry at the same time by choosing a specific surface orientation [13, 15] provides us the opportunity to investigate the magnetoelectric effect [3, 16]. However, despite tremendous theoretical and experimental efforts to find new AFM-TIs in single crystalline form [17–19], obtaining good quality AFM-TI materials is very challenging.

Very recently, one of the magnetic variants of well-studied Bi_2Te_3 family 3D TIs [20, 21] - $MnBi_2Te_4$ - has been theoretically proposed to be an intrinsically stoichiometric AFM-TI, where the novel Z_2 topological invariant was protected by the S symmetry in the A-type AFM configuration [17, 22–30]. Its unusual electronic structure opens a route to study different variants of topological phenomena including 2D and 3D magnetic interaction, quantum anomalous Hall effect (QAH), axion states, chiral Majorana modes and an elusive single pair of Weyl nodes near the Fermi level [31–34]. Such peculiar properties of the electronic states can be realized in $MnBi_2Te_4$ by breaking the S symmetry on the (0001) surface [22]. As $MnBi_2Te_4$ is built of the stacking blocks of Te-Bi-Te-Mn-Te-Bi-Te septuple layers, breaking the S symmetry can be achieved by cleavage sample surface along (0001) direction in the AFM state or by inducing a transition from AFM to a state with a finite total moment, induced by an external magnetic field. The magnetic structure with A-type AFM order is required for the occurrence of the gap in the 2D surface Dirac cone [22],. Indeed, in the bulk the $MnBi_2Te_4$ exhibits AFMA order, which recently has been verified by neutron diffraction [35]. Although multiple experimental results of $MnBi_2Te_4$ reported a Dirac surface state with a gap opening of 50 to 200 meV [25, 26, 34] at low temperatures, no significant change was observed across the AFM transition [25]. These results contradict to the other theoretical predictions and call for further detailed study.

Here, we present high-resolution ARPES data and first-principles calculations to investigate the surface states and bulk properties of $MnBi_2Te_4$. In stark contrast to the earlier ARPES findings of a surface state with a band gap ranging from 50 to 200 meVs [25, 26, 34], we find a gapless Dirac surface states at the Γ point of the Brillouin zone. In addition, we identified another 2D Dirac point with a binding energy of 40 meV on the

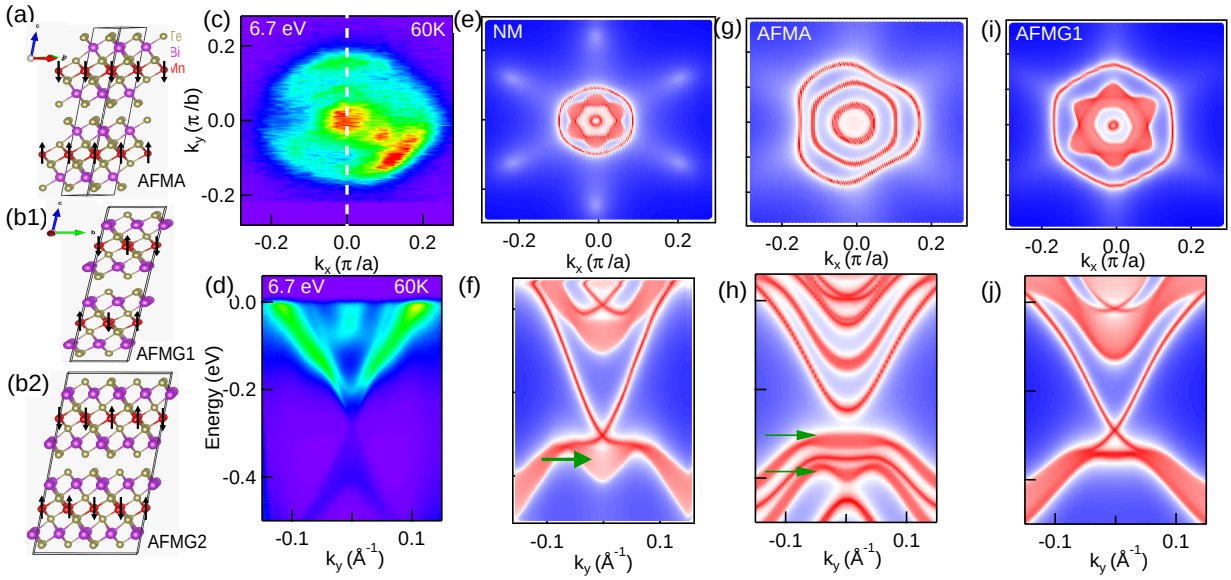

FIG. 1. Crystal and electronic structure of $MnBi_2Te_4$. (a) Crystal structure of $MnBi_2Te_4$ (Mn, red spheres; Bi, purple spheres; Te, gold spheres) with A-type AFM (AFMA) configurations. (b1, b2) Single- and double-row G-type AFM (AFMG1, AFMG2) configurations. (c) Fermi surface plot - ARPES intensity integrated within 10 meV about the chemical potential measured using 6.7 eV photons at 60 K. (d) Band dispersion along the high symmetry line as shown in (c). (e) Calculated Fermi surface of $MnBi_2Te_4$ with non-magnetic (NM) configuration (Mn replaced with Zn) using a semi-infinite (0001) surface. (f) Calculated electronic structure of $MnBi_2Te_4$ with NM configuration along the white dashed line in (c). (g) Calculated Fermi surface of $MnBi_2Te_4$ with AFMA configuration using a semi-infinite (0001) surface. (h) Calculated electronic structure of $MnBi_2Te_4$ with AFMA configuration along the white dashed line in (c). (i) Calculated Fermi surface of $MnBi_2Te_4$ with AFMG1 configuration using a semi-infinite (0001) surface. (j) Calculated electronic structure of $MnBi_2Te_4$ with AFMG1 configuration along the white dashed line in (c). The green arrows in (f) and (h) point to the bulk band and splittings in DFT calculations.

same (0001) surface, which has not been reported in any other measurements yet. Surprisingly, these gapless surface states did not open up gaps as the sample undergoes AFM transition, raising the question whether the sample is indeed an AFM-TI with A-type AFM configuration or not. Our detailed DFT calculations with different magnetic moment configurations, point to a possibility that AFM G-type moments configurations at the surface (single- or double-row) support gapless surface states on the (0001) surface as the effective S symmetry is preserved along the b direction. Thus, the gapless surface states would not react to the bulk magnetic phase transition. $MnBi_2Te_4$ is therefore a unique platform for studying the interplay of magnetism and topological phases.

Single crystals of $MnBi_2Te_4$ were grown out of a Bi-Te flux [35]. Platelike samples used for ARPES measurements were cleaved *in situ* at 60 K under ultra-high vacuum (UHV). The data were acquired using a tunable VUV laser ARPES system, that consists of a Omicron Scienta DA30 electron analyzer, a picosecond Ti:Sapphire oscillator and fourth harmonic generator [36]. Data were collected with photon energies of 6.7 and 6.36 eV. Momentum and energy resolutions were set at ~ 0.005 Å^{-1} and 2 meV. The size of the photon beam on the sample was $\sim$30 μm.

Band structures with spin-orbit coupling (SOC) in density functional theory (DFT) [37, 38] have been calculated using a PBE [39] exchange-correlation functional, a plane-wave basis set and projector augmented wave method [40] as implemented in VASP [41, 42]. To account for the half-filled strongly localized Mn 3d orbitals, a Hubbard-like U [43] value of 3.0 eV is used. For bulk band structure of A-type anti-ferromagnetic (AFMA) $MnBi_2Te_4$, the rhombohedral unit cell is doubled along c direction with a Monkhorst-Pack [44] ($9 \times 9 \times 3$) k-point mesh including the Γ point and a kinetic energy cutoff of 270 eV. The band structure of the G-type anti-ferromagnetic (AFMG) configuration is calculated by further doubling the rhombohedral unit cell in the other two directions. Experimental lattice parameters [45] have been used with atoms fixed in their bulk positions. A tight-binding model based on maximally localized Wannier functions [46–48] was constructed to reproduce closely the bulk band structure including SOC in the range of $E_F \pm 1$ eV with Mn sd, Bi p and Te p orbitals. Then the spectral functions and Fermi surface of a semi-infinite $MnBi_2Te_4$ (0001) surface were calculated with the surface Greens function methods [49–52] as implemented in WannierTools [53].

Figure 1(a) shows the crystal structure and A-type

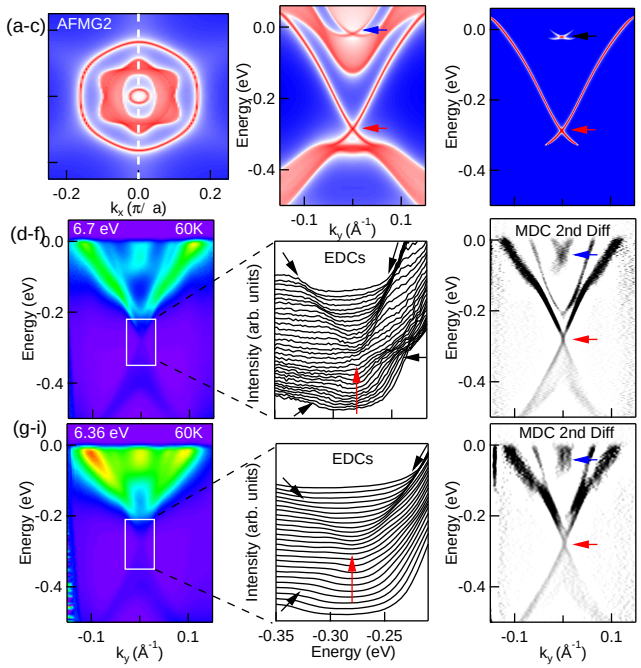

FIG. 2. Fermi surface plot and band dispersions of $MnBi_2Te_4$. (a) Calculated Fermi surface of $MnBi_2Te_4$ with double row G-type AFM (AFMG2) configuration using a semi-infinite (001) surface. (b) Calculated electronic structure of $MnBi_2Te_4$ along the white dashed line in (a). (c) Surface states extracted from (b). (d) Band dispersion along the white dashed line in (a) measured using 6.7 eV photons at 60 K. (e) Energy Distribution Curves (EDCs) corresponding to the white solid box in panel (d). The black arrows trace the peak locations of the EDCs. (f) Second derivatives of ARPES intensity map in panel (d) with respect to MDC. (g) Band dispersion along the white dashed line in (a) measured using 6.36 eV photons at 60 K. (h) Energy Distribution Curves (EDCs) corresponding to the white solid box in panel (g). The black arrows trace the peak locations of the EDCs. (i) Second derivatives of ARPES intensity map in panel (g) with respect to MDC. The blue [black in (c)] and red arrows in panels (c), (e), (f), (h), and (i) point to the first and second Dirac point at two binding energies, respectively.

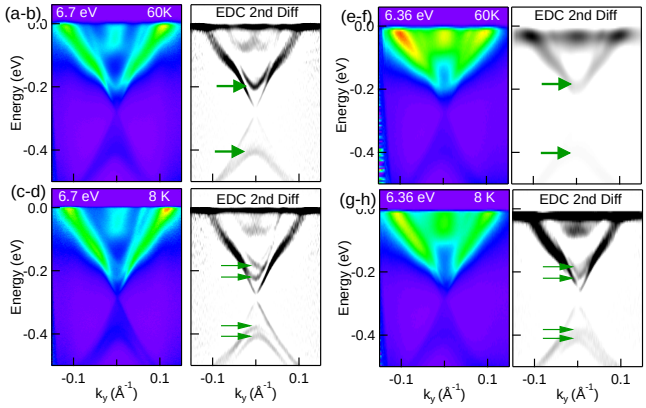

FIG. 3. Temperature evolution of the band dispersions measured using 6.7 and 6.36 eV. (a) Band dispersion along the white dashed line in Fig. 2(a) measured using 6.7 eV photons at 60 K. (b) Second derivative of ARPES intensity map in panel (a) with respect to EDC. (c-d) Similar to (a-b) but measured at 8 K. (e) Band dispersion along the white dashed line in Fig. 2(a) measured using 6.36 eV photons at 60 K. (f) Second derivative of ARPES intensity map in panel (a) with respect to EDC. (g-h) Similar to (e-f) but measured at 8 K. Green arrows in panels (d) and (h) point to the splitting of the bulk bands under magnetic transition.

AFM (AFMA) magnetic orderings of $MnBi_2Te_4$. Single- and double-row G-type AFM (AFMG1 and AFMG2) configurations can be generated by doubling the rhombohedral unit cell and reversing the magnetic moments alignment in the neighboring unit cells in the other two directions as shown in Figs. 1(b1) and (b2). In the AFMA configuration, the S symmetry is broken on the (0001) surface. However, in both AFMG1 and AFMG2 configurations, breaking only the symmetry along c axis on the (0001) surface does not gap out the Dirac point, because the symmetries from two other directions (i.e. along a and b axis) still remain. Thus, these two configurations would lead to gapless topological surface states on this surface. Fig. 1(c) shows the ARPES intensity plots of $MnBi_2Te_4$ measured using 6.7 eV photons at 60 K. Two shallow electron pockets and a blob of intensity can be seen at the Γ point. Fig. 1(d) shows the band dispersion along the white dashed line in panel (c), where two large and one shallow electron pocket can be easily identified. Surprisingly, a gapless Dirac state is clearly present, which remains intact as the sample undergoes AFM transition at 24 K (Fig. 3). This observation is in stark contrast to the previous predictions and ARPES results showing gapped out Dirac dispersion at the Γ point [17, 22–28]. To elucidate the origin of this gapless Dirac state, we conducted DFT calculations on three types of magnetic moment configurations: AFMA, AFMG1, and AFMG2 (Fig. 2). Figures (e) and (f) shows the Fermi surface and band dispersion from DFT calculations with Mn atoms replaced by Zn atoms in $MnBi_2Te_4$ to model the non-magnetic (NM) state. We can clearly see the gapless surface states in panel (f), which is consistent with the ARPES results shown in panel (d). Since we do not see any significant changes to the surface states in the ARPES measurements as the sample undergoes AFM transition (Fig. 3), we are going to show the DFT calculations in the AFM configurations for comparison. In Figs. 1(g) and (h), we can see that the band dispersion from DFT calculations shows a gapped Dirac surface state as the material undergoes AFMA transition, leading to the AFM topological insulator state, which is inconsistent with the ARPES data. Whereas the bulk states pointed by the green arrows in panels (f) and (h) show a clear bulk band splitting, which will be discussed in more detail in Fig. 3. On the

other hand, with the AFMG1 or AFMG2 configurations, the Fermi surface and band dispersion from DFT calculations reproduce the ARPES intensity pretty well as shown in Figs. 1(i-j) and 2(a-b). In order to achieve a better match between DFT and ARPES results, we have to shift the chemical potential of DFT calculations upwards by roughly 220 meV, which is probably due to the lattice defects [35]. Recent inelastic neutron scattering and DFT+U study [54] shows that significant intralayer next-nearest-neighbor (NNN) AFM coupling could bring frustration for intralayer magnetic configurations. In our DFT+U calculations, the single-row AFMG1 configuration is 4.7 meV/f.u. higher than AFMA, but the double-row AFMG2 is significantly more stable with only 1.9 meV/f.u. above. This shows that different magnetic configurations due to frustration [54] are indeed accessible and shows consistency with our ARPES results.

In Fig. 2, we presented the DFT calculations and ARPES intensities of $MnBi_2Te_4$ in great detail. Fig. 2(c) shows the surface state contribution extracted from the DFT calculation results shown in panel (b), which clearly separates the surface v.s. bulk states in DFT calculations. Other than the Dirac point marked by the red arrow, we can also identify another Dirac point marked by the blue arrow in panels (b) and (c), which has not been reported by other ARPES studies yet. These surface Dirac states are protected by the effective TRS in the AFMG configurations, which has yet to be accounted for. We should also note that the absence of a gap in the Dirac surface states could be due to other reasons such as weak magnetic coupling between bulk and surface states. To demonstrate that these two Dirac surface states indeed exist in the ARPES spectra, we plotted the raw data of Energy Distribution Curves (EDCs) and the second derivative of ARPES intensity with respect to momentum distribution curve (MDC) in panels (e) and (f). In panel (e) we can clearly trace the EDC peaks (black arrows) to the Dirac point located at E_B=-280 meV, whereas in panel (f) we can clearly see two distinct Dirac points at the binding energies of 40 and 280 meV as marked by the blue and red arrows, respectively. Both Dirac surface states reside in the gaps of the bulk continuum and connect the bulk conduction and valence bands, signaling their topological nature. The good correspondence between the ARPES features and the DFT calculations can easily help us separate the bulk vs surface contributions in the ARPES spectra. Similar features can be identified in the ARPES intensity measured using 6.36 eV photons at 60 K, as shown in panels (h) and (i). The slight movement in the binding energy of the inner parabolic band with respect to photon energy change demonstrates its bulk origin. The consistency between the DFT calculations and ARPES intensities clearly demonstrate that there are two instead of just one gapless Dirac surface states on the (0001) surface in $MnBi_2Te_4$.

Next, let's focus on the temperature evolution of the electronic structure in $MnBi_2Te_4$ as shown in Fig. 3. Panel (b) shows the second derivative of the ARPES intensity calculated with respect to EDC measured using 6.7 eV at 60 K (above the T_N = 24 K). Other than the two gapless Dirac surface states identified in Fig. 2, we can also observe parabolic conduction and valence bands marked by the green arrows as shown in panel (b). Upon cooling the sample temperature down to 8 K below the AFM transition temperature [panels (c)-(d)], we can see that the single conduction band splits into two bands as marked by the two green arrows close to the binding energy of 200 meV in panel (d). The same happened to the valence band sitting at E_B=400 meV measured using both 6.7 and 6.36 eV photons as shown in panels (d) and (h), respectively. Since $MnBi_2Te_4$ undergoes an AFM instead of FM transition, this splitting of the band is probably due to the bulk-surface interlayer ferromagnetic coupling. Recent inelastic neutron scattering and DFT+U study [54] shows that the interlayer AFM coupling is actually weaker than the intralayer NNN AFM coupling. Since AFMC configuration, i.e. FM along c axis and AFM along a or b axis, also has a relatively small energy cost (5.02 meV/f.u.) and is accessible, we also considered this and found that it results in gapless Dirac surface states and no bulk band splitting, similar to the results in AFMG configurations. Thus, the band splitting is likely attributed to the FM interaction in the AFMA configuration as shown in Fig 1. Meanwhile, the two gapless Dirac surface states does not seem to be correlated with the bulk AFM transition, implicating that the surface may indeed have a different configuration from the bulk [55] or have a weak magnetic coupling with the bulk states. Although the sample undergoes AFM transition with possible AFMG configuration, in-plane band folding due to the in-plane doubling from AFMA to AFMG then to AFMG2 was not observed. This is because the topological features arise from band inversion around Γ point between Te and Bi p_z orbitals, which are not affected much by the in-plane doubling except for the effective TRS consideration.

In conclusion, we presented high-resolution ARPES data and first-principles calculations to investigate the electronic properties of $MnBi_2Te_4$. In contrast to the observation of gapped surface state at the Γ point from earlier ARPES measurements [25, 26, 34], we observed two gapless topological surface states with Dirac points sitting at roughly 40 and 280 meV below Fermi level. Furthermore, these gapless Dirac surface states do not evolve along with the magnetic transition. This is despite clear evidence for AFMA ordering in the bulk [35], which indicates weak coupling of the surface state to bulk magnetism. As the samples most likely cleaved between the adjacent Bi_2Te_3 layers with Mn layer well protected from depletion due to cleaving, the gapless surface states is unliely due to Mn-poor surface regions. On the other

hand, recent inelastic neutron scattering and DFT+U study [54] shows that there is a significant intralayer NNN AFM coupling, which brings frustration for intralayer magnetic configurations. Therefore, our findings provide interesting results for $MnBi_2Te_4$ and demonstrate that it could be a unique platform for studying the interplay of magnetism and topological features.

Upon completion of this project we become aware that other groups [29, 56–58] independently studied $MnBi_2Te_4$ and showed an indication of a single gapless surface Dirac cone in this compound.

We would like to thank Peter Orth and Robert McQueeney for very insightful discussions. Research at Ames Laboratory and ORNL was supported by the U.S. Department of Energy, Office of Basic Energy Sciences, Division of Materials Science and Engineering. P. S and Y. W were supported by the Center for the Advancement of Topological Semimetals, an Energy Frontier Research Center funded by the U.S. DOE, Office of Basic Energy Sciences. Ames Laboratory is operated for the U.S. Department of Energy by Iowa State University under Contract No. DE-AC02-07CH11358. B. S. was supported by CEM, a NSF MRSEC, under Grant No. DMR-1420451.

Relevant data for the work are available at the Materials Data Facility [59].

* yanj@ornl.gov
† kaminski@ameslab.gov

[1] M. Z. Hasan and C. L. Kane, Rev. Mod. Phys. **82**, 3045 (2010).
[2] N. P. Armitage, E. J. Mele, and A. Vishwanath, Rev. Mod. Phys. **90**, 015001 (2018).
[3] Y. Tokura, K. Yasuda, and A. Tsukazaki, Nature Reviews Physics **1**, 126 (2019).
[4] E. Gibney, Nature **560**, 151 (2018).
[5] C.-K. Chiu, J. C. Y. Teo, A. P. Schnyder, and S. Ryu, Rev. Mod. Phys. **88**, 035005 (2016).
[6] L. Plucinski, Journal of Physics: Condensed Matter **31**, 183001 (2019).
[7] L. M. Schoop, F. Pielnhofer, and B. V. Lotsch, Chemistry of Materials **30**, 3155 (2018).
[8] M. A. Bandres, S. Wittek, G. Harari, M. Parto, J. Ren, M. Segev, D. N. Christodoulides, and M. Khajavikhan, Science **359**, eaar4005 (2018).
[9] S. Manipatruni, D. E. Nikonov, C.-C. Lin, T. A. Gosavi, H. Liu, B. Prasad, Y.-L. Huang, E. Bonturim, R. Ramesh, and I. A. Young, Nature **565**, 35 (2019).
[10] L. Šmejkal, Y. Mokrousov, B. Yan, and A. H. MacDonald, Nature Physics **14**, 242 (2018).
[11] D. Pesin and A. H. MacDonald, Nature Materials **11**, 409 (2012).
[12] M. Jamali, J. S. Lee, J. S. Jeong, F. Mahfouzi, Y. Lv, Z. Zhao, B. K. Nikolić, K. A. Mkhoyan, N. Samarth, and J.-P. Wang, Nano Letters **15**, 7126 (2015).
[13] R. S. K. Mong, A. M. Essin, and J. E. Moore, Phys. Rev. B **81**, 245209 (2010).
[14] J. E. Moore, Nature (London) **464**, 194 (2010).
[15] A. M. Essin, J. E. Moore, and D. Vanderbilt, Phys. Rev. Lett. **102**, 146805 (2009).
[16] N. P. Armitage and L. Wu, SciPost Phys. **6**, 46 (2019).
[17] J. Li, Y. Li, S. Du, Z. Wang, B.-L. Gu, S.-C. Zhang, K. He, W. Duan, and Y. Xu, Science Advances **5**, eaaw5685 (2019).
[18] Y. Xu, Z. Song, Z. Wang, H. Weng, and X. Dai, Phys. Rev. Lett. **122**, 256402 (2019).
[19] L.-L. Wang, N. H. Jo, B. Kuthanazhi, Y. Wu, R. J. McQueeney, A. Kaminski, and P. C. Canfield, Phys. Rev. B **99**, 245147 (2019).
[20] Y. L. Chen, J. G. Analytis, J.-H. Chu, Z. K. Liu, S.-K. Mo, X. L. Qi, H. J. Zhang, D. H. Lu, X. Dai, Z. Fang, S. C. Zhang, I. R. Fisher, Z. Hussain, and Z.-X. Shen, Science **325**, 178 (2009).
[21] R. Jiang, L.-L. Wang, M. Huang, R. S. Dhaka, D. D. Johnson, T. A. Lograsso, and A. Kaminski, Phys. Rev. B **86**, 085112 (2012).
[22] M. M. Otrokov, I. I. Klimovskikh, H. Bentmann, A. Zeugner, Z. S. Aliev, S. Gass, A. U. B. Wolter, A. V. Koroleva, D. Estyunin, A. M. Shikin, M. Blanco-Rey, M. Hoffmann, A. Y. Vyazovskaya, S. V. Eremeev, Y. M. Koroteev, I. R. Amiraslanov, M. B. Babanly, N. T. Mamedov, N. A. Abdullayev, V. N. Zverev, B. Büchner, E. F. Schwier, S. Kumar, A. Kimura, L. Petaccia, G. D. Santo, R. C. Vidal, S. Schatz, K. Kißner, C.-H. Min, S. K. Moser, T. R. F. Peixoto, F. Reinert, A. Ernst, P. M. Echenique, A. Isaeva, and E. V. Chulkov, arXiv:1809.07389 (2018).
[23] Y. Gong, J. Guo, J. Li, K. Zhu, M. Liao, X. Liu, Q. Zhang, L. Gu, L. Tang, X. Feng, D. Zhang, W. Li, C. Song, L. Wang, P. Yu, X. Chen, Y. Wang, H. Yao, W. Duan, Y. Xu, S.-C. Zhang, X. Ma, Q.-K. Xue, and K. He, Chinese Physics Letters **36**, 076801 (2019).
[24] M. M. Otrokov, I. P. Rusinov, M. Blanco-Rey, M. Hoffmann, A. Y. Vyazovskaya, S. V. Eremeev, A. Ernst, P. M. Echenique, A. Arnau, and E. V. Chulkov, Phys. Rev. Lett. **122**, 107202 (2019).
[25] A. Zeugner, F. Nietschke, A. U. B. Wolter, S. Gaß, R. C. Vidal, T. R. F. Peixoto, D. Pohl, C. Damm, A. Lubk, R. Hentrich, S. K. Moser, C. Fornari, C. H. Min, S. Schatz, K. Kißner, M. Ünzelmann, M. Kaiser, F. Scaravaggi, B. Rellinghaus, K. Nielsch, C. Hess, B. Büchner, F. Reinert, H. Bentmann, O. Oeckler, T. Doert, M. Ruck, and A. Isaeva, Chemistry of Materials **31**, 2795 (2019).
[26] R. C. Vidal, H. Bentmann, T. R. F. Peixoto, A. Zeugner, S. Moser, C. H. Min, S. Schatz, K. Kissner, M. Ünzelmann, C. I. Fornari, H. B. Vasili, M. Valvidares, K. Sakamoto, J. Fujii, I. Vobornik, T. K. Kim, R. J. Koch, C. Jozwiak, A. Bostwick, J. D. Denlinger, E. Rotenberg, J. Buck, M. Hoesch, F. Diekmann, S. Rohlf, M. Kalläne, K. Rossnagel, M. M. Otrokov, E. V. Chulkov, M. Ruck, A. Isaeva, and F. Reinert, arXiv:1903.11826 (2019).
[27] J. Q. Yan, S. Okamoto, M. A. McGuire, A. F. May, R. J. McQueeney, and B. C. Sales, arXiv:1905.00400 (2019).
[28] J. Li, C. Wang, Z. Zhang, B.-L. Gu, W. Duan, and Y. Xu, arXiv:1905.00642 (2019).
[29] B. Chen, F. Fei, D. Zhang, B. Zhang, W. Liu, S. Zhang, P. Wang, B. Wei, Y. Zhang, Z. Zuo, J. Guo, Q. Liu, Z. Wang, X. Wu, J. Zong, X. Xie, W. Chen, Z. Sun, S. Wang, Y. Zhang, M. Zhang, X. Wang, F. Song, H. Zhang, D. Shen, and B. Wang, Nature Communications **10**, 4469 (2019).

[30] P. Rani, A. Saxena, R. Sultana, V. Nagpal, S. Patnaik, and V. Awana, arXiv preprint arXiv:1906.09038 (2019).

[31] D. Zhang, M. Shi, T. Zhu, D. Xing, H. Zhang, and J. Wang, Phys. Rev. Lett. **122**, 206401 (2019).

[32] C. Liu, Y. Wang, H. Li, Y. Wu, Y. Li, J. Li, K. He, Y. Xu, J. Zhang, and Y. Wang, arXiv:1905.00715 (2019).

[33] N. Varnava and D. Vanderbilt, Phys. Rev. B **98**, 245117 (2018).

[34] S. H. Lee, Y. Zhu, Y. Wang, L. Miao, T. Pillsbury, S. Kempinger, D. Graf, N. Alem, C.-Z. Chang, N. Samarth, and Z. Mao, arXiv:1812.00339 (2018).

[35] J.-Q. Yan, Q. Zhang, T. Heitmann, Z. Huang, K. Y. Chen, J.-G. Cheng, W. Wu, D. Vaknin, B. C. Sales, and R. J. McQueeney, Phys. Rev. Materials **3**, 064202 (2019).

[36] R. Jiang, D. Mou, Y. Wu, L. Huang, C. D. McMillen, J. Kolis, H. G. Giesber, J. J. Egan, and A. Kaminski, Review of Scientific Instruments **85**, 033902 (2014).

[37] P. Hohenberg and W. Kohn, Phys. Rev. **136**, B864 (1964).

[38] W. Kohn and L. J. Sham, Phys. Rev. **140**, A1133 (1965).

[39] J. P. Perdew, K. Burke, and M. Ernzerhof, Phys. Rev. Lett. **77**, 3865 (1996).

[40] P. E. Blöchl, Phys. Rev. B **50**, 17953 (1994).

[41] G. Kresse and J. Furthmüller, Phys. Rev. B **54**, 11169 (1996).

[42] G. Kresse and J. Furthmüller, Computational Materials Science **6**, 15 (1996).

[43] S. L. Dudarev, G. A. Botton, S. Y. Savrasov, C. J. Humphreys, and A. P. Sutton, Phys. Rev. B **57**, 1505 (1998).

[44] H. J. Monkhorst and J. D. Pack, Phys. Rev. B **13**, 5188 (1976).

[45] D. S. Lee, T.-H. Kim, C.-H. Park, C.-Y. Chung, Y. S. Lim, W.-S. Seo, and H.-H. Park, CrystEngComm **15**, 5532 (2013).

[46] N. Marzari and D. Vanderbilt, Phys. Rev. B **56**, 12847 (1997).

[47] I. Souza, N. Marzari, and D. Vanderbilt, Phys. Rev. B **65**, 035109 (2001).

[48] N. Marzari, A. A. Mostofi, J. R. Yates, I. Souza, and D. Vanderbilt, Rev. Mod. Phys. **84**, 1419 (2012).

[49] D. H. Lee and J. D. Joannopoulos, Phys. Rev. B **23**, 4988 (1981).

[50] D. H. Lee and J. D. Joannopoulos, Phys. Rev. B **23**, 4997 (1981).

[51] M. P. L. Sancho, J. M. L. Sancho, and J. Rubio, Journal of Physics F: Metal Physics **14**, 1205 (1984).

[52] M. P. L. Sancho, J. M. L. Sancho, J. M. L. Sancho, and J. Rubio, Journal of Physics F: Metal Physics **15**, 851 (1985).

[53] Q. Wu, S. Zhang, H.-F. Song, M. Troyer, and A. A. Soluyanov, arXiv preprint arXiv:1703.07789 (2017).

[54] J.-Q. Yan, D. Pajerowski, L. Ke, A. Nedić, Y. Sizyuk, E. Gordon, P. Orth, D. Vaknin, and R. McQueeney, arXiv preprint arXiv:1908.02332 (2019).

[55] D. Mou, A. Sapkota, H.-H. Kung, V. Krapivin, Y. Wu, A. Kreyssig, X. Zhou, A. I. Goldman, G. Blumberg, R. Flint, and A. Kaminski, Phys. Rev. Lett. **116**, 196401 (2016).

[56] Y.-J. Hao, P. Liu, Y. Feng, X.-M. Ma, E. F. Schwier, M. Arita, S. Kumar, C. Hu, R. Lu, M. Zeng, Y. Wang, Z. Hao, H.-Y. Sun, K. Zhang, J. Mei, N. Ni, L. Wu, K. Shimada, C. Chen, Q. Liu, and C. Liu, Phys. Rev. X **9**, 041038 (2019).

[57] Y. J. Chen, L. X. Xu, J. H. Li, Y. W. Li, H. Y. Wang, C. F. Zhang, H. Li, Y. Wu, A. J. Liang, C. Chen, S. W. Jung, C. Cacho, Y. H. Mao, S. Liu, M. X. Wang, Y. F. Guo, Y. Xu, Z. K. Liu, L. X. Yang, and Y. L. Chen, Phys. Rev. X **9**, 041040 (2019).

[58] H. Li, S.-Y. Gao, S.-F. Duan, Y.-F. Xu, K.-J. Zhu, S.-J. Tian, J.-C. Gao, W.-H. Fan, Z.-C. Rao, J.-R. Huang, J.-J. Li, D.-Y. Yan, Z.-T. Liu, W.-L. Liu, Y.-B. Huang, Y.-L. Li, Y. Liu, G.-B. Zhang, P. Zhang, T. Kondo, S. Shin, H.-C. Lei, Y.-G. Shi, W.-T. Zhang, H.-M. Weng, T. Qian, and H. Ding, Phys. Rev. X **9**, 041039 (2019).

[59] DOI:xxxxx.xxxxxx.